GNSS-BASED POSITIONING

Robust Vehicular Localization and Map Matching in Urban Environments Through IMU, GNSS, and Cellular Signals

**Zaher (Zak) M. Kassas, Mahdi Maaref, Joshua J. Morales,
Joe J. Khalife, and Kimia Shamaei**
*Are with the University of California, Irvine and the Autonomous Systems Perception, Intelligence, and Navigation Laboratory, University of California, Irvine.
Email: zkassas@ieee.org; mmaaref@uci.edu; joshum9@uci.edu;
khalifej@uci.edu; and kshamaei@uci.edu*

Abstract—A framework for ground vehicle localization that uses cellular signals of opportunity (SOPs), a digital map, an inertial measurement unit (IMU), and a Global Navigation Satellite System (GNSS) receiver is developed. This framework aims to enable localization in an urban environment where GNSS signals could be unusable or unreliable. The proposed framework employs an extended Kalman filter (EKF) to fuse pseudorange observables extracted from cellular SOPs, IMU measurements, and GNSS-derived position estimates (when available). The EKF is coupled with a map-matching approach. The framework assumes the positions of the cellular towers to be known, and it estimates the vehicle's states (position, velocity, orientation, and IMU biases) along with the difference between the vehicle-mounted receiver clock error states (bias and drift) and each cellular SOP clock error state. The proposed framework is evaluated experimentally on a ground vehicle navigating in a deep urban area with a limited sky view. Results show a position root-mean-square error (RMSE) of 2.8 m across a 1,380-m trajectory when GNSS signals are available and an RMSE of 3.12 m across the same trajectory when GNSS signals are unavailable for 330 m. Moreover, compared to localization with a loosely coupled GNSS–IMU integrated system, a 22% reduction in the localization error is obtained whenever GNSS signals are available, and an 81% reduction in the localization error is obtained whenever GNSS signals are unavailable.

*Digital Object Identifier 10.1109/MITS.2020.2994110
Date of current version: 22 June 2020*

©ISTOCKPHOTO/TAMPATRA

1939-1390/20©2020IEEE

Localization technologies for navigation and ground vehicle autonomy levels have been evolving hand in hand. Ten years ago, ground vehicle localization systems for navigation consisted of a GPS receiver, a wheel odometer, and an inertial measurement unit (IMU). Localization errors greater than lane-level and periodic dropouts of the navigation solution were tolerable to the driver, who had to follow the path drawn on the GPS navigation system. Although localization and some form of path planning from a start location to a desired destination were performed autonomously, the driver had to steer the car, control acceleration, avoid obstacles, change lanes, and so on. Today, as ground vehicles evolve by incorporating autonomous-type driving technologies (e.g., cruise control, active steering, collision avoidance, lane detection, and so on), the requirements for localization and navigation technologies become more stringent, necessitating the need for additional sensors (lidar, vision, radar, among others). Large errors become less acceptable, and the consistent availability of the navigation solution is critical.

For example, it is not enough to estimate on which freeway the vehicle is driving, as certain autonomous actions require lane-level localization. This is crucial for intersections, exiting or entering a freeway, and at a junction of different freeways or streets. Moreover, when entering the freeway, for instance, the navigation solution must be continuously available to ensure the safety of passengers and other drivers. Looking ahead, as ground vehicles are endowed with full autonomy, the robustness and accuracy of their localization and navigation systems become of paramount importance. Without a human driver-in-the-loop, one does not expect to have to question the availability of the localization and navigation systems, which must provide predictable performance in different driving scenarios.

Despite the promise of Global Navigation Satellite System (GNSS) signals as an accurate sensing modality, in GNSS-challenged environments (e.g., deep urban streets), these signals suffer from different error sources, including multipath, signal blockage due to a limited sky view, uncertainties in satellite clocks and positions, signal propagation delays in the ionosphere and troposphere, user receiver noise, and so on. In such conditions, it is imperative to continuously monitor the integrity of GNSS signals. *Integrity monitoring* refers to the capability of the system to detect GNSS anomalies and warn the user when the system should not employ GNSS measurements [1]. Integrity monitoring frameworks are divided into internal and external categories [2]. External methods leverage a network of ground monitoring stations to observe the transmitted signals, while internal methods (e.g., receiver autonomous integrity monitoring) typically use the redundant information within the transmitted navigation signals.

As shown in [3], the navigation framework can be coupled with these integrity monitoring methods to detect GNSS unreliability and unavailability. In addition to unavailability due to anomalies, GNSS signals may become inaccessible in jamming or spoofing situations. It is also often the case that GNSS receivers lose track of the signals in multipath or non-line-of-sight (NLOS) environments, making the GNSS position solution unreliable. In such cases, an integrity monitoring system would alert the user of an unreliable or unavailable position solution. Such integrity monitoring frameworks can be adapted for cellular-based navigation, the details of which can be found in [4].

Traditional vehicular localization and navigation technologies were heavily dependent on GNSS receivers. During the past decade, these systems evolved by coupling GNSS receivers with onboard sensors, such as IMUs. Moreover, such navigation systems may have access to proximity localization techniques (e.g., lidar, camera, and radar), which provide local position information and aid in collision avoidance. Map-matching techniques have also been developed to fit the direction-finding solution obtained by the navigation system to a point on the digital map [3], [5], [6]. More recently, signals of opportunity (SOPs) have been fused with GNSS receivers to complement the GNSS navigation solution [7] or as an alternative to the GNSS [8].

This article considers, for the first time, the fusion of the preceding readily available, off-the-shelf technologies to achieve a highly robust and accurate navigation solution in urban environments by complementing the individual technologies' desirable attributes. Specifically, the developed system uses:

- *GNSS*: The GNSS can provide a meter- and submeter-level accurate navigation solution using code and carrier phase measurements, respectively, in a global frame. However, GNSS signals are highly attenuated indoors and in deep urban canyons, which makes them practically unusable in these environments. Moreover, GNSS signals are sensitive to multipath and susceptible to intentional interference (jamming) and counterfeit signals (spoofing), which can wreak havoc in military and civilian applications.
- *IMUs*: While IMU sensors provide an accurate short-term navigation solution, one cannot rely on them as a stand-alone accurate solution for long-term navigation. This is due to the fact that the noisy outputs of IMUs are integrated through an inertial navigation system (INS), causing pose estimation errors to accumulate through time [9], [10]. The accumulated error rate is dependent on the quality of the IMU. These errors compromise the safe and efficient operation requirements for ground vehicle navigation in urban environments. Thus, for long-term navigation, an IMU sensor becomes unreliable, and an aiding source is needed to correct its drift and improve the navigation solution.

- *Cellular SOPs*: Cellular base transceiver stations (BTSs) are abundant and available in several bands, aggregating to tens of megahertz of usable cellular radio-frequency spectrum, making them robust against jamming and spoofing attacks as well as service outages in certain bands or providers. The cellular system BTS configuration, through the construction of the hexagonal cells, possesses favorable geometry, which yields a low horizontal dilution of precision. The received carrier-to-noise ratio from nearby cellular BTSs is commonly tens of decibels higher than that of GNSS space vehicle (SV) signals, making these signals usable for localization purposes in urban environments. However, due to the low elevation angles of cellular towers compared to GNSS SVs, received cellular signals are affected by multipath (e.g., due to buildings, trees, poles, other vehicles, and so on). Nevertheless, cellular signals have a large bandwidth (up to 20 MHz), which is useful to the receiver in detecting and alleviating multipath effects, leading to precise time-of-arrival (TOA) estimates and, in turn, a precise navigation solution.
- *Map matching*: Map matching for ground vehicle navigation has been extensively studied [5], [11]–[14]. It has been shown that a map-matching framework can provide integrity at the lane level [3]. Map matching can also correct sensor errors [15]–[17]. Moreover, it has been shown that digital map information can be used to correct the accumulated error in dead-reckoning-type sensors (e.g., IMUs) [18]. However, digital maps may have displacement errors.

This article presents a robust vehicular localization framework for navigating in both GNSS-available and GNSS-denied urban environments. When GNSS signals are unavailable or compromised, the framework extracts navigation observables from cellular signals and fuses them with IMU and map data to continuously estimate the vehicle's states. When GNSS signals are available, the navigation solution is obtained by fusing the IMU data, map data, cellular signals, and GNSS-derived position estimate.

The proposed framework was tested in different environments with a performance comparable (within 2–3 m) to that of an expensive high-end system that uses a dual-frequency GNSS with real-time kinematics (RTK) and a tactical-grade IMU. The proposed approach does not rely on the GNSS for ground vehicle navigation in urban environments. Instead, it exploits the abundance of ambient cellular SOPs in such areas. It is worth noting that the GNSS suffers from other issues beyond a lack of coverage, such as severe multipath in deep urban canyons and susceptibility to jamming and spoofing. However, the focus of this article is to develop a low-cost system that performs well without the GNSS, which could be unavailable or unreliable for whatever reason.

Initial work that considered fusing map data and cellular signals was conducted in [19], where ground vehicle navigation in GNSS-denied environments was studied. This article extends the work in [19] through the following contributions. First, [19] did not consider any onboard navigation sensors, while this article formulates a realistic course-plotting framework for a vehicle equipped with an IMU. Second, [19] provided a thorough study with many simulation and experimental results, which examined the performance of the framework under different driving conditions, such as turning along the road, crossing junctions, and coming to a complete stop. In contrast, this article focuses on technological and algorithmic aspects and explores the robustness of the proposed framework in challenging environments (e.g., a setting where both the GNSS and cellular signals are highly attenuated by tall trees and buildings).

Third, [19] employs a particle filter, whereas in this article, the proposed system uses a computationally efficient extended Kalman filter (EKF) to fuse digital map data, IMU data, the estimated position using an off-the-shelf GNSS receiver, and cellular SOP pseudoranges. Fourth, in contrast to [19], this article is written in a tutorial fashion that offers sufficient details about the proposed system in addition to references for the interested reader to probe for further details. It is worth noting that the proposed framework in this article does not specifically assume RTK-type GNSS-derived position estimates. Instead, it considers a low-cost GNSS receiver, producing a navigation solution with meter-level accuracy.

Figure 1 presents a high-level diagram of the proposed ground vehicle localization system. The cellular-aided IMU block and the map-matching block are demonstrated in this figure. In contrast to existing map-matching approaches, the proposed algorithm is closed-loop, where the navigation solution is fed back to correct estimates of the receiver and cellular SOP clock error states. To account for the unmodeled map's errors (e.g., the map's displacement error), the proposed framework finds the smallest Mahalanobis distance between the map points and the vehicle's estimated position, where the inaccuracies in the map are modeled as a random vector with a known mean and covariance. Note that the problems of localization and navigation are not isolated from each other but, rather, closely linked. If a vehicle does not know its exact position at the start of a planned trajectory, it will encounter problems in reaching the destination [20]. Hence, in the following, the term *navigation* is applied to both localization and navigation purposes.

To evaluate the performance of the proposed ground vehicle navigation algorithm, two experimental tests were performed using ambient cellular LTE SOPs in 1) an urban environment where signal attenuation severely affects the received pseudoranges and 2) an environment where SOPs have poor geometric diversity. Experimental results with the proposed method are presented, illustrating a close match between the vehicle's true trajectory and the estimated one using the cellular-aided IMU plus map data, particularly in a GNSS-denied environment with a limited LOS to the open sky. The experimental results demonstrate a position root-mean-square error (RMSE) of 2.8 m across a 1,380-m trajectory with available GNSS signals and an RMSE of 3.12 m across the same trajectory when GNSS signals were unavailable for 330 m.

Moreover, it is demonstrated that incorporating the proposed algorithm reduces the position RMSE by 22% and 81% in GNSS-available and GNSS-denied environments, respectively, from the RMSE obtained by a GNSS–IMU navigation solution. The achieved results are also compared with the outcomes in [19] (i.e., a particle filter-based framework without using the IMU sensor). It is demonstrated that the proposed method achieves a maximum error of 5.03 m in an environment with poor SOP geometric diversity, whereas the method in [19] produces a maximum error of 11.7 m in the same environment. Hence, adopting the proposed method reduces the maximum error by 57%.

Navigation Framework Model Description

This section describes the models of the different components of the vehicular navigation framework: the IMU, cellular SOP, GNSS receiver, and digital map.

IMU Measurement Model

An IMU produces measurements of the angular rate and specific force. To use these measurements, the IMU's orientation, position, velocity, and measurement biases must be estimated. In this work, an IMU state vector $\boldsymbol{x}_v$ consisting of 16 states is used, and it is given by

$$\boldsymbol{x}_v = [{}^I_G\bar{\boldsymbol{q}}^\top, \boldsymbol{p}_v^\top, \dot{\boldsymbol{p}}_v^\top, \boldsymbol{b}_g^\top, \boldsymbol{b}_a^\top]^\top, \tag{1}$$

where ${}^I_G\bar{\boldsymbol{q}}$ is a 4D unit quaternion representing the IMU's orientation (i.e., rotation from a global frame G to the IMU's body frame I), where frame G is set to be an inertial frame, such as the Earth-centered inertial frame; $\boldsymbol{p}_v \triangleq [p_{v,x}, p_{v,y}, p_{v,z}]^\top$ and $\dot{\boldsymbol{p}}_v$ are the 3D position and velocity of the vehicle, respectively, expressed in G; and $\boldsymbol{b}_g$ and $\boldsymbol{b}_a$ are the 3D gyroscope and accelerometer biases, respectively. The IMU's measurements of the angular rate $\boldsymbol{\omega}$ and specific force $\mathbf{a}$ are available every T seconds and can be modeled as

$$\boldsymbol{\omega} = {}^I\boldsymbol{\omega} + \boldsymbol{b}_g + \boldsymbol{n}_g, \tag{2}$$

$$\mathbf{a} = \mathbf{R}[{}^I_G\bar{\boldsymbol{q}}]({}^G\mathbf{a}_I - {}^G\boldsymbol{g}) + \boldsymbol{b}_a + \boldsymbol{n}_a, \tag{3}$$

respectively, where ${}^I\boldsymbol{\omega}$ is the IMU's true rotation rate; $\boldsymbol{n}_g$ is a measurement noise vector, which is modeled as a white noise sequence with covariance $\mathbf{Q}_g$; $\mathbf{R}[{}^I_G\bar{\boldsymbol{q}}]$ is the equivalent rotation matrix of ${}^I_G\bar{\boldsymbol{q}}$; ${}^G\mathbf{a}_I$ is the IMU's true acceleration in frame G; and $\boldsymbol{n}_a$ is a measurement noise vector, which is modeled as a white noise sequence with covariance $\mathbf{Q}_a$. The evolution of the gyroscope and accelerometer biases are modeled as random walks; i.e., $\dot{\boldsymbol{b}}_a = \boldsymbol{w}_a$ and $\dot{\boldsymbol{b}}_g = \boldsymbol{w}_g$, where $\boldsymbol{w}_a$ and $\boldsymbol{w}_g$ are modeled as zero-mean random vectors with covariances $\sigma^2_{w_a}\mathbf{I}_{3\times3}$ and $\sigma^2_{w_g}\mathbf{I}_{3\times3}$, respectively, where $\mathbf{I}_{n\times n}$ denotes an $n \times n$ identity matrix. The equivalent rotation matrix $\mathbf{R}[\bar{\boldsymbol{q}}]$ of the quaternion vector $\bar{\boldsymbol{q}} = [q_0, q_{v_1}, q_{v_2}, q_{v_3}]^\top$ is

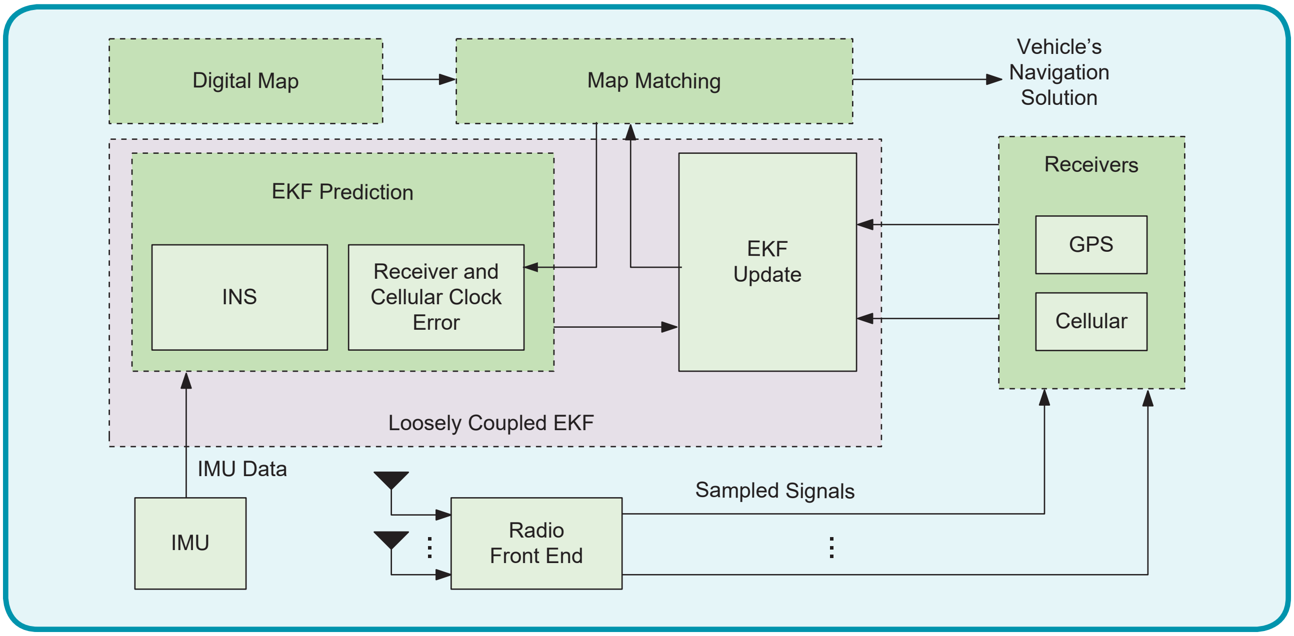

FIG 1 A high-level diagram of the cellular-aided IMU framework in which the outputs of the IMU are fused in a loosely coupled fashion. The navigation solution obtained from the map-matching block is fed back to correct estimates of the receiver's and the cellular SOPs clock error states.

$$\mathbf{R}[\bar{\boldsymbol{q}}] = [\boldsymbol{r}_1, \boldsymbol{r}_2, \boldsymbol{r}_3], \quad \boldsymbol{r}_1 = \begin{bmatrix} q_0^2 + q_{v_1}^2 - q_{v_2}^2 - q_{v_3}^2 \\ 2(q_{v_1}q_{v_2} - q_0 q_{v_3}) \\ 2(q_{v_1}q_{v_3} + q_0 q_{v_2}) \end{bmatrix},$$

$$\boldsymbol{r}_2 = \begin{bmatrix} 2(q_{v_1}q_{v_2} + q_0 q_{v_3}) \\ q_0^2 - q_{v_1}^2 + q_{v_2}^2 - q_{v_3}^2 \\ 2(q_{v_2}q_{v_3} - q_0 q_{v_1}) \end{bmatrix},$$

$$\boldsymbol{r}_3 = \begin{bmatrix} 2(q_{v_1}q_{v_3} - q_0 q_{v_3}) \\ 2(q_{v_2}q_{v_3} + q_0 q_{v_1}) \\ q_0^2 - q_{v_1}^2 - q_{v_2}^2 + q_{v_3}^2 \end{bmatrix}.$$

The measurements in (2) and (3) will be used in the EKF to perform a time update of the estimate of $\boldsymbol{x}_v$ between measurement updates. This will be discussed in the "EKF Time Update" section.

GNSS Receiver Measurement Model

The GNSS receiver is assumed to estimate the vehicle-mounted receiver's 3D position according to

$$\hat{\boldsymbol{p}}_{\text{GNSS}} = \boldsymbol{p}_v + \boldsymbol{w}_{\text{GNSS}},$$

where $\boldsymbol{w}_{\text{GNSS}}$ models the uncertainty about this estimate, which is modeled as a zero-mean Gaussian random vector with covariance $\boldsymbol{\Sigma}_g = \text{diag}[\sigma^2_{\text{GNSS},x}, \sigma^2_{\text{GNSS},y}, \sigma^2_{\text{GNSS},z}]$. Note that $\boldsymbol{\Sigma}_g$ consists of different error sources, including satellite and receiver clock errors, satellites' orbit errors, and ionospheric and tropospheric delays, but not multipath. It is important to mention that in addition to GNSS unavailability due to anomalies, GNSS signals may become unavailable in the case where the GNSS receiver loses the signal track in severe multipath conditions or when there is a very low carrier-to-noise ratio. Therefore, navigating in severe multipath environments (e.g., deep urban canyons), requires modeling and accounting for the multipath in addition to calculating Σ_g. Multipath modeling is beyond the scope of this article; however, it has been the subject of many studies [21], [22]. Relevant work in the literature surveyed different multipath mitigation techniques [23]–[25]. These models may be used to construct the multipath contribution to GNSS-based position estimates, accordingly. More details are available in [19].

Cellular SOP Received Signal Model

Cellular towers transmit signals for synchronization and channel estimation purposes. These signals can be used to deduce the pseudorange between the transmitting tower and the receiver. In code-division multiple access systems, a pilot signal consisting of a pseudorandom noise sequence, known as the short code, is modulated by a carrier signal and broadcast by each BTS for synchronization purposes [26]. Therefore, by knowing the short code, the receiver can measure the code phase of the pilot signal as well as its carrier phase, hence forming a pseudorange measurement to each BTS transmitting the pilot signal [27], [28].

Two types of positioning techniques can be defined for LTE, namely, network-based and user equipment (UE)-based positioning. In network-based positioning, a positioning reference signal (PRS) is broadcast by the Evolved Node B (eNodeB) [29]. The UE uses the PRS to measure the pseudoranges to multiple eNodeBs and transfers the measurements to the network, where the location of the UE is estimated. During the past several years, research has focused on UE-based positioning techniques, where the broadcast reference signals—namely, the primary synchronization signal, secondary synchronization signal, and cell-specific reference signal (CRS)—were explained for navigation purposes [30]. Among these sequences, it was demonstrated that the CRS yields the most precise positioning, due to its large transmission bandwidth [31]. The CRS is transmitted to estimate the channel between the UE and the eNodeB and could have a bandwidth of up to 20 MHz. Several techniques have been proposed to extract the TOA from the CRS, such as 1) threshold-based approaches [32], [33], 2) the superresolution algorithm [34], and 3) software-defined receivers [35], [36]. Experimental results have shown meter-level positioning accuracy using stand-alone LTE CRS signals (i.e., without fusing other sensors).

In a very dynamic environment, e.g., for a moving receiver, the channel coherence time is relatively small (less than the measurement's sampling time). Therefore, in a LOS condition, the pseudorange error due to multipath can be modeled with a zero-mean white Gaussian sequence, and an additive Gaussian noise model is valid for LTE pseudorange measurements. In an NLOS scenario, the receiver tracks the multipath signal instead of the LOS. Therefore, a nonzero bias must be added to the pseudorange measurement model. Researchers have proposed multiple NLOS-identification methods, including cooperative and noncooperative techniques [37]. When a NLOS measurement is detected, the receiver can either exclude it from the measurement set or reduce the measurement's weight to decrease the error due to the NLOS signal [37]. NLOS identification is beyond the scope of this research, and all measurements are considered to be LOS.

A model of the LOS pseudorange made by the receiver on the nth cellular SOP is given by [38]

$$\begin{aligned} z_{\text{sop},n}(k) = {} & \|\boldsymbol{p}_v(k) - \boldsymbol{p}_{\text{sop},n}\|_2 + c \cdot [\delta t_r(k) - \delta t_{\text{sop},n}(k)] \\ & + v_{\text{sop},n}(k), \\ & n = 1, \ldots, N_{\text{sop}}, \end{aligned}$$

where N_{sop} is the total number of available cellular SOPs; $\boldsymbol{p}_{\text{sop},n}$ and $\delta t_{\text{sop},n}$ are the 3D position vector and the clock bias of the nth cellular SOP transmitter, respectively; $\boldsymbol{p}_v$ and δt_r are the 3D position of vehicle and the receiver's clock bias, respectively; and $v_{\text{sop},n}$ is the measurement noise, which is modeled as a zero-mean white Gaussian sequence with variance $\sigma^2_{\text{sop},n}$. Note that the pseudorange measurement noise variance includes both the effect of noise and multipath error. Since cellular SOP transmitters are stationary, their positions $\{\boldsymbol{p}_{\text{sop},n}\}_{n=1}^{N_{\text{sop}}}$ could be readily obtained, e.g., from cellular tower location databases or by mapping them a priori [39], [40].

The proposed framework assumes a priori knowledge of $\{\boldsymbol{p}_{\text{sop},n}\}_{n=1}^{N_{\text{sop}}}$. Note that, in general, some cellular SOP transmitter positions tend to overlap due to having base stations from multiple carrier providers on the same physical tower. In this article, only one cellular SOP is taken from a physical tower location; hence, $\{\boldsymbol{p}_{\text{sop},n}\}_{n=1}^{N_{\text{sop}}}$ are all different. By virtue of the hexagonal cellular system structure, cellular SOPs from different tower locations tend to be distributed fairly uniformly around the receiver, which significantly reduces the dilution of the precision [40]. Optimal performance is obtained when the SOPs form a regular polygon around the receiver when $N_{\text{sop}} \geq 3$ [41]. It was observed from several data sets of LTE signals recorded in vehicular environments that typical values of N_{sop} vary between three and five for each operator. The 3rd Generation Partnership Project 2 protocol requires cellular base stations to be synchronized to within 10 μs from the GPS time [42]. Cellular base stations are typically equipped with GNSS receivers to meet this synchronization requirement.

While this level of synchronization is acceptable for communication purposes, it might introduce significant errors (on the order of tens of meters) in the pseudorange measurements if not accounted for properly, which, in turn, introduces large errors in the navigation solution. Therefore, each cellular SOP is assumed to have its own clock error states, namely, clock bias and drift. Moreover, the SOP clock biases are stochastic and dynamic; hence, they must be continuously estimated. The vehicle-mounted receiver clock error state vector is $\boldsymbol{x}_{\text{clk},r} \triangleq [\delta t_r, \dot{\delta t}_r]^{\mathsf{T}}$, where $\dot{\delta t}_r$ is the receiver's clock drift, and the nth cellular SOP clock error state vector is $\boldsymbol{x}_{\text{clk,sop},n} \triangleq [\delta t_{\text{sop},n}, \dot{\delta t}_{\text{sop},n}]^{\mathsf{T}}$, where $\dot{\delta t}_{\text{sop},n}$ is the transmitter's clock drift [43]. The discrete-time dynamics of $\boldsymbol{x}_{\text{clk},r}$ and $\boldsymbol{x}_{\text{clk,sop},n}$ are given by

$$\boldsymbol{x}_{\text{clk},r}(k+1) = \mathbf{F}_{\text{clk}} \boldsymbol{x}_{\text{clk},r}(k) + \boldsymbol{w}_{\text{clk},r}(k), \tag{4}$$

$$\boldsymbol{x}_{\text{clk,sop},n}(k+1) = \mathbf{F}_{\text{clk}} \boldsymbol{x}_{\text{clk,sop},n}(k) + \boldsymbol{w}_{\text{clk,sop},n}(k), \tag{5}$$

where $\boldsymbol{w}_{\text{clk},r}$ and $\boldsymbol{w}_{\text{clk,sop},n}$ are zero-mean white random sequences with covariances $\mathbf{Q}_{\text{clk},r}$ and $\mathbf{Q}_{\text{clk,sop},n}$, respectively, and

$$\mathbf{F}_{\text{clk}} = \begin{bmatrix} 1 & T \\ 0 & 1 \end{bmatrix},$$

$$\mathbf{Q}_{\text{clk},r} = \begin{bmatrix} S_{\tilde{w}_{\delta t,r}} T + S_{\tilde{w}_{\dot{\delta t},r}} \frac{T^3}{3} & S_{\tilde{w}_{\dot{\delta t},r}} \frac{T^2}{2} \\ S_{\tilde{w}_{\dot{\delta t},r}} \frac{T^2}{2} & S_{\tilde{w}_{\dot{\delta t},r}} T \end{bmatrix},$$

where T is the sampling time; $S_{\tilde{w}_{\delta t,r}}$ and $S_{\tilde{w}_{\dot{\delta t},r}}$ are the power spectra of the continuous-time equivalent-process noise driving the vehicle-mounted receiver's clock bias and drift, respectively; and $\mathbf{Q}_{\text{clk,sop},n}$ has the same form as $\mathbf{Q}_{\text{clk},r}$, except that $S_{\tilde{w}_{\delta t,r}}$ and $S_{\tilde{w}_{\dot{\delta t},r}}$ are replaced with the nth cellular SOP-specific spectra $S_{\tilde{w}_{\delta t,\text{sop},n}}$ and $S_{\tilde{w}_{\dot{\delta t},\text{sop},n}}$, respectively. The detailed derivations of the clock bias and the drift-process noise power spectral densities are described in [44]–[46].

It is important to mention that the pseudorange measurements drawn from the SOP transmitters are parameterized by the difference between the SOPs' and the receiver's clock bias [43]. Therefore, estimating $\boldsymbol{x}_{\text{clk},r}$ and $\boldsymbol{x}_{\text{clk,sop},n}$ individually is unnecessary in this framework; instead, the difference $\Delta \boldsymbol{x}_{\text{clk,sop},n} = c \cdot (\boldsymbol{x}_{\text{clk},r} - \boldsymbol{x}_{\text{clk,sop},n}) \triangleq [c\Delta\delta t_{\text{sop},n}, c\Delta\dot{\delta t}_{\text{sop},n}]^{\mathsf{T}}$ is estimated, where $c\Delta\delta t_{\text{sop},n} \triangleq c \cdot [\delta t_r - \delta t_{\text{sop},n}]$ and $c\Delta\dot{\delta t}_{\text{sop},n} \triangleq c \cdot [\dot{\delta t}_r - \dot{\delta t}_{\text{sop},n}]$. The augmented clock error state is defined as

$$\boldsymbol{x}_{\text{clk,sop}} \triangleq [\Delta \boldsymbol{x}_{\text{clk,sop},1}^{\mathsf{T}}, \ldots, \Delta \boldsymbol{x}_{\text{clk,sop},N_{\text{sop}}}^{\mathsf{T}}]^{\mathsf{T}}. \tag{6}$$

It can be readily seen that $\boldsymbol{x}_{\text{clk,sop}}$ evolves according to the discrete-time dynamics

$$\boldsymbol{x}_{\text{clk,sop}}(k+1) = \boldsymbol{\Phi}_{\text{clk}} \boldsymbol{x}_{\text{clk,sop}}(k) + \boldsymbol{w}_{\text{clk,sop}}(k), \tag{7}$$

where $\boldsymbol{\Phi}_{\text{clk}} \triangleq \text{diag}[\mathbf{F}_{\text{clk}}, \ldots, \mathbf{F}_{\text{clk}}]$ and $\boldsymbol{w}_{\text{clk,sop}}$ is a zero-mean white random sequence with covariance $\mathbf{Q}_{\text{clk,sop}}$ given by

$$\mathbf{Q}_{\text{clk,sop}} = c^2 \begin{bmatrix} \mathbf{Q}_{\text{clk,sop},r,1} & \mathbf{Q}_{\text{clk},r} & \ldots & \mathbf{Q}_{\text{clk},r} \\ \mathbf{Q}_{\text{clk},r} & \mathbf{Q}_{\text{clk,sop},r,2} & \ldots & \mathbf{Q}_{\text{clk},r} \\ \vdots & \vdots & \ddots & \vdots \\ \mathbf{Q}_{\text{clk},r} & \mathbf{Q}_{\text{clk},r} & \ldots & \mathbf{Q}_{\text{clk,sop},r,N_{\text{sop}}} \end{bmatrix},$$

where

$$\mathbf{Q}_{\text{clk,sop},r,i} \triangleq \mathbf{Q}_{\text{clk,sop},i} + \mathbf{Q}_{\text{clk},r}, \quad \text{for } i = 1, \ldots, N_{\text{sop}}.$$

Map Model

The primary function of digital map technology is to produce a chart that provides a precise representation of points of interest (e.g., road networks) in a particular area. Digital maps collect and process landscape information and compile the coordinates of geographical objects. During recent years, incorporating digital maps for accurate vehicle guidance has been the subject of many studies [15]–[17], which resulted in the development of so-called map-matching techniques. *Map matching* refers to the process of associating the vehicle's estimated position with the spatial information extracted from the digital map [3], [47]. Map-matching algorithms employ a priori information concerning geographical features to enhance the vehicle's navigation solution by localizing the car within the road network.

The framework presented in this article uses the open source digital map available on the Open Street Map (OSM) database [48]. The road networks are extracted using a MATLAB parser, which interpolates coordinates between points that have a horizontal distance greater than a predefined threshold. The elevation profile of the road is obtained using Google Earth. Figure 2 summarizes the steps to extract map-matched points from a digital map. Figure 2(a) shows the navigation environment in Riverside, California. Figure 2(b) demonstrates the same area in the OSM database, which is downloadable from the OSM website [48]. Figure 2(c)–(e) conveys the steps to process the map data and extract the coordinates of the road. Finally, Figure 2(f) illustrates the map-matched points before and after interpolation. This area contains 144,670 map-matched points and 185 roads, which are indicated in Figure 2(f) through red circles and blue lines, respectively.

The proposed framework accounts for inaccuracies in the map by incorporating a 3D displacement error $\boldsymbol{w}_m$, which is modeled as a zero-mean random vector with covariance $\boldsymbol{\Sigma}_m = \mathrm{diag}[\sigma^2_{m_x}, \sigma^2_{m_y}, \sigma^2_{m_z}]$. To this end, the smallest Mahalanobis distance between the map points and the vehicle's estimated position is calculated at each time step k, and the vehicle's position is refined accordingly. This is discussed in the "Map Matching and Closed-Loop Clock Error State Correction" section.

Data Fusion and Map-Matching Framework

This section describes an EKF-based framework to fuse IMU measurements with GNSS and cellular pseudoranges to estimate the vehicle's states (1) and clock error states (6). The framework also employs a closed-loop map-matching step to refine the estimates of the clock error states. A vehicle equipped with an IMU described in the "IMU Measurement Model" section is assumed to navigate in an environment comprising N_{sop} cellular SOP transmitters with fully known locations. The framework provides robust and accurate navigation with and without GNSS signals by exploiting ambient cellular SOPs. In contrast to traditional approaches, which employ an integrated GNSS–IMU system with a digital map, the proposed framework deals with unknown dynamic stochastic error states of cellular SOPs by simultaneously estimating them. These estimates are further refined via a closed-loop map-matching step. The EKF time and measurement update steps are outlined next, followed by the map-matching correction step.

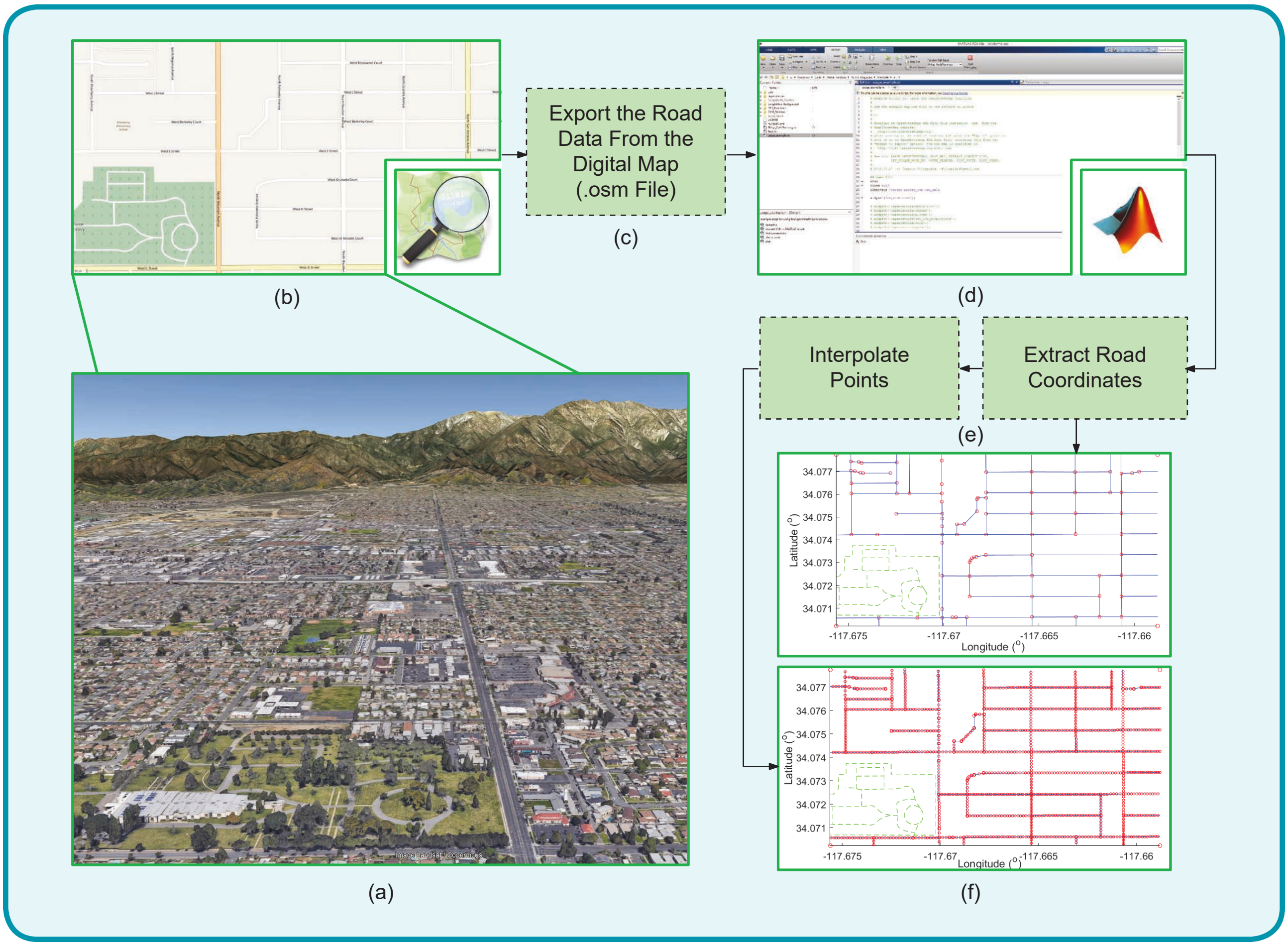

FIG 2 The steps to extract the map-matched points from a digital map. (a) The navigation environment. (b) The OSM digital map (available at www.openstreetmap.org). (c) Exporting the.osm file, which contains road data. (d) The MATLAB-based parser to extract road data from the.osm file. (e) Processing the digital map, including extracting the road coordinates and interpolating points between successive map-matched points with a distance greater than a specified threshold. (f) The map-matched points before (top) and after (bottom) interpolation.

EKF Time Update

In this section, the EKF time update step is described. The EKF's vector $\boldsymbol{x}$ consists of the vehicle's state $\boldsymbol{x}_v$ (1) and the clock error states (6), i.e.,

$$\boldsymbol{x} = [\boldsymbol{x}_v^{\mathsf{T}}, \boldsymbol{x}_{\mathrm{clk,sop}}^{\mathsf{T}}]^{\mathsf{T}}.$$

The cellular SOPs are assumed to be stationary with known positions $\{\boldsymbol{p}_{\mathrm{sop},n}\}_{n=1}^{N_{\mathrm{sop}}}$. Between measurement updates (whether from the GNSS or cellular signals), the IMU's sampled measurements of the angular velocity $\boldsymbol{\omega}$ and linear acceleration $\mathbf{a}$ are used to perform a time update of $\hat{\boldsymbol{x}}(k|j)$ for $k \geq j$, which denotes the estimate of $x(k)$ using all measurements up to time step j, to get the predicted states $\hat{\boldsymbol{x}}(k+1|j)$ and corresponding prediction error covariance $\mathbf{P}(k+1|j)$. The time update of the orientation state estimate is given by

$$ {}^{I_{k+1|j}}_{G}\hat{\bar{\boldsymbol{q}}} = {}^{I_{k+1}}_{I_k}\hat{\bar{\boldsymbol{q}}} \otimes {}^{I_{k|j}}_{G}\hat{\bar{\boldsymbol{q}}}, \tag{8}$$

where ${}^{I_{k+1}}_{I_k}\hat{\bar{\boldsymbol{q}}}$ represents the estimated relative rotation of the IMU from time step k to $k+1$. In (8), $\otimes$ denotes the quaternion multiplication operator, which functions on two quaternion vectors $\boldsymbol{q}_1 \triangleq [q_{0,1}, q_{v_1,1}, q_{v_2,1}, q_{v_3,1}]$ and $\boldsymbol{q}_2 \triangleq [q_{0,2}, q_{v_1,2}, q_{v_2,2}, q_{v_3,2}]$ to yield

$$\begin{aligned}\boldsymbol{q}_1 \otimes \boldsymbol{q}_2 = [&q_{0,1}q_{0,2} - q_{v_1,1}q_{v_1,2} - q_{v_2,1}q_{v_2,2} - q_{v_3,1}q_{v_3,2},\\ &q_{0,1}q_{v_1,2} + q_{v_1,1}q_{0,2} + q_{v_2,1}q_{v_3,2} - q_{v_3,1}q_{v_2,2},\\ &q_{0,1}q_{v_2,2} - q_{v_1,1}q_{v_3,2} + q_{v_2,1}q_{0,2} + q_{v_3,1}q_{v_1,2},\\ &q_{0,1}q_{v_3,2} + q_{v_1,1}q_{v_2,2} - q_{v_2,1}q_{v_1,2} + q_{v_3,1}q_{0,2}]^{\mathsf{T}}.\end{aligned}$$

The value of ${}^{I_{k+1}}_{I_k}\hat{\bar{\boldsymbol{q}}}$ is found by integrating the measurements $\boldsymbol{\omega}(k)$ and $\boldsymbol{\omega}(k+1)$ using a fourth-order Runge–Kutta, which yields

$$\begin{aligned}&{}^{I_{k+1}}_{I_k}\hat{\bar{\boldsymbol{q}}} = \bar{\boldsymbol{q}}_0 + \frac{T}{2}(\boldsymbol{d}_1 + 2\boldsymbol{d}_2 + 2\boldsymbol{d}_3 + \boldsymbol{d}_4),\\ &\quad \boldsymbol{d}_1 = \frac{1}{2}\boldsymbol{\Omega}(\hat{\boldsymbol{\omega}}(k))\bar{\boldsymbol{q}}_0, \quad \boldsymbol{d}_2 = \frac{1}{2}\boldsymbol{\Omega}(\hat{\bar{\boldsymbol{\omega}}}(k))\Big(\bar{\boldsymbol{q}}_0 + \frac{1}{2}T\boldsymbol{d}_1\Big),\\ &\quad \boldsymbol{d}_3 = \frac{1}{2}\boldsymbol{\Omega}(\hat{\bar{\boldsymbol{w}}}(k))\Big(\bar{\boldsymbol{q}}_0 + \frac{1}{2}T\boldsymbol{d}_2\Big),\\ &\quad \boldsymbol{d}_4 = \frac{1}{2}\boldsymbol{\Omega}(\hat{\boldsymbol{\omega}}(k+1))\Big(\bar{\boldsymbol{q}}_0 + \frac{1}{2}T\boldsymbol{d}_3\Big),\\ &\hat{\bar{\boldsymbol{\omega}}}(k) = \frac{1}{2}(\hat{\boldsymbol{\omega}}(k) + \hat{\boldsymbol{\omega}}(k+1)), \quad \bar{\boldsymbol{q}}_0 = [1, 0, 0, 0]^{\mathsf{T}},\end{aligned}$$

where $\hat{\boldsymbol{\omega}} = \boldsymbol{\omega} - \hat{\boldsymbol{b}}_g$ and

$$\boldsymbol{\Omega}(\boldsymbol{\omega}) = \begin{bmatrix} 0 & \boldsymbol{\omega}^{\mathsf{T}} \\ \boldsymbol{\omega} & \lfloor \boldsymbol{\omega} \times \rfloor \end{bmatrix},$$

$$\lfloor \boldsymbol{\omega} \times \rfloor = \begin{bmatrix} 0 & -\omega_z & \omega_y \\ \omega_z & 0 & -\omega_x \\ -\omega_y & \omega_x & 0 \end{bmatrix}, \quad \boldsymbol{\omega} = [\omega_x, \omega_y, \omega_z]^{\mathsf{T}}.$$

The time update of the velocity estimate is computed using the trapezoidal integration according to

$$\hat{\dot{\boldsymbol{p}}}_v(k+1|j) = \hat{\dot{\boldsymbol{p}}}_v(k|j) + \frac{T}{2}[\hat{\mathbf{s}}(k) + \hat{\mathbf{s}}(k+1)] + T^G\boldsymbol{g}(k), \tag{9}$$

where $\hat{\mathbf{s}}(k) \triangleq \mathbf{R}_{\hat{q}}^{\mathsf{T}}(k)\hat{\boldsymbol{a}}(k)$, $\hat{\boldsymbol{a}}(k) \triangleq \boldsymbol{a}(k) - \hat{\boldsymbol{b}}_a(k|j)$, and $\mathbf{R}_{\hat{q}}(k) \triangleq \mathbf{R}\Big[{}^{I_{k|j}}_{G}\hat{\bar{\boldsymbol{q}}}\Big]$. The time update of the position estimate is given by

$$\hat{\boldsymbol{p}}_v(k+1|j) = \hat{\boldsymbol{p}}_v(k|j) + \frac{T}{2}[\hat{\dot{\boldsymbol{p}}}_v(k+1|j) + \hat{\dot{\boldsymbol{p}}}_v(k|j)]. \tag{10}$$

The time update of the gyroscope and accelerometer biases estimates is given by

$$\hat{\boldsymbol{b}}_g(k+1|j) = \hat{\boldsymbol{b}}_g(k|j), \quad \hat{\boldsymbol{b}}_a(k+1|j) = \hat{\boldsymbol{b}}_a(k|j). \tag{11}$$

The time update of the clock error state estimate is readily deduced from (7) to be given by

$$\hat{\boldsymbol{x}}_{\mathrm{clk,sop}}(k+1|j) = \boldsymbol{\Phi}_{\mathrm{clk}}\hat{\boldsymbol{x}}_{\mathrm{clk,sop}}(k|j). \tag{12}$$

The time update of the prediction error covariance is given by

$$\begin{aligned}\mathbf{P}(k+1|j) &= \mathbf{F}(k)\mathbf{P}(k|j)\mathbf{F}^{\mathsf{T}}(k) + \mathbf{Q}(k), \qquad (13)\\ \mathbf{F}(k) &\triangleq \mathrm{diag}[\boldsymbol{\Phi}_B(k+1,k), \boldsymbol{\Phi}_{\mathrm{clk}}],\\ \mathbf{Q}(k) &\triangleq \mathrm{diag}[\mathbf{Q}_{d_B}(k), \mathbf{Q}_{\mathrm{clk,sop}}].\end{aligned}$$

The discrete-time INS state transition matrix $\boldsymbol{\Phi}_B$ and process noise covariance $\mathbf{Q}_{d_B}$ are computed using standard INS equations, as described in [49] and [50].

Remark

The 4D quaternion vector is an over-determined representation of the orientation state. To avoid singularities due to this over-determined representation, the estimation error covariance of the three Euler angles is maintained in the EKF. Therefore, the block pertaining to the orientation state in $\mathbf{P}(k|j)$ is 3 × 3.

EKF Measurement Update

When GNSS signals are available, the EKF measurement update stage corrects the time-updated states using cellular SOP pseudoranges, data obtained from the map, and the estimated position provided by the GNSS $\hat{\boldsymbol{p}}_{\mathrm{GNSS}}$. Here, the measurement vector $\mathcal{Z}(k)$ consists of $\hat{\boldsymbol{p}}_{\mathrm{GNSS}}$ and $\{z_{\mathrm{sop},n}\}_{n=1}^{N_{\mathrm{sop}}}$, where $z_{\mathrm{sop},n}$ is the pseudorange drawn from the nth cellular SOP transmitter.

When GNSS signals are cut off, the measurement update stage uses only cellular SOP pseudoranges and digital map data. Here, $\mathcal{Z}(k)$ includes only cellular SOP measurements, $\{z_{\mathrm{sop},n}\}_{n=1}^{N_{\mathrm{sop}}}$. Next, the corrected state estimate $\hat{\boldsymbol{x}}(k+1|k+1)$ and the associated estimation error covariance $\mathbf{P}(k+1|k+1)$ are computed using the standard EKF measurement update equations [45]. The expressions of the corresponding measurement Jacobian $\mathbf{H}$ and the measurement noise covariance $\boldsymbol{\Sigma}_s$ are demonstrated in Figure 3.

Map Matching and Closed-Loop Clock Error State Correction

Assuming that the digital map comprises L_N locations, denoted $\{\boldsymbol{l}_n \triangleq [p_{mx_n}, p_{my_n}, p_{mz_n}]^{\mathsf{T}}\}_{n=1}^{L_N}$, the position estimate $\hat{\boldsymbol{p}}_v(k|k)$ is map-matched to yield $\hat{\boldsymbol{p}}_m(k|k)$ according to

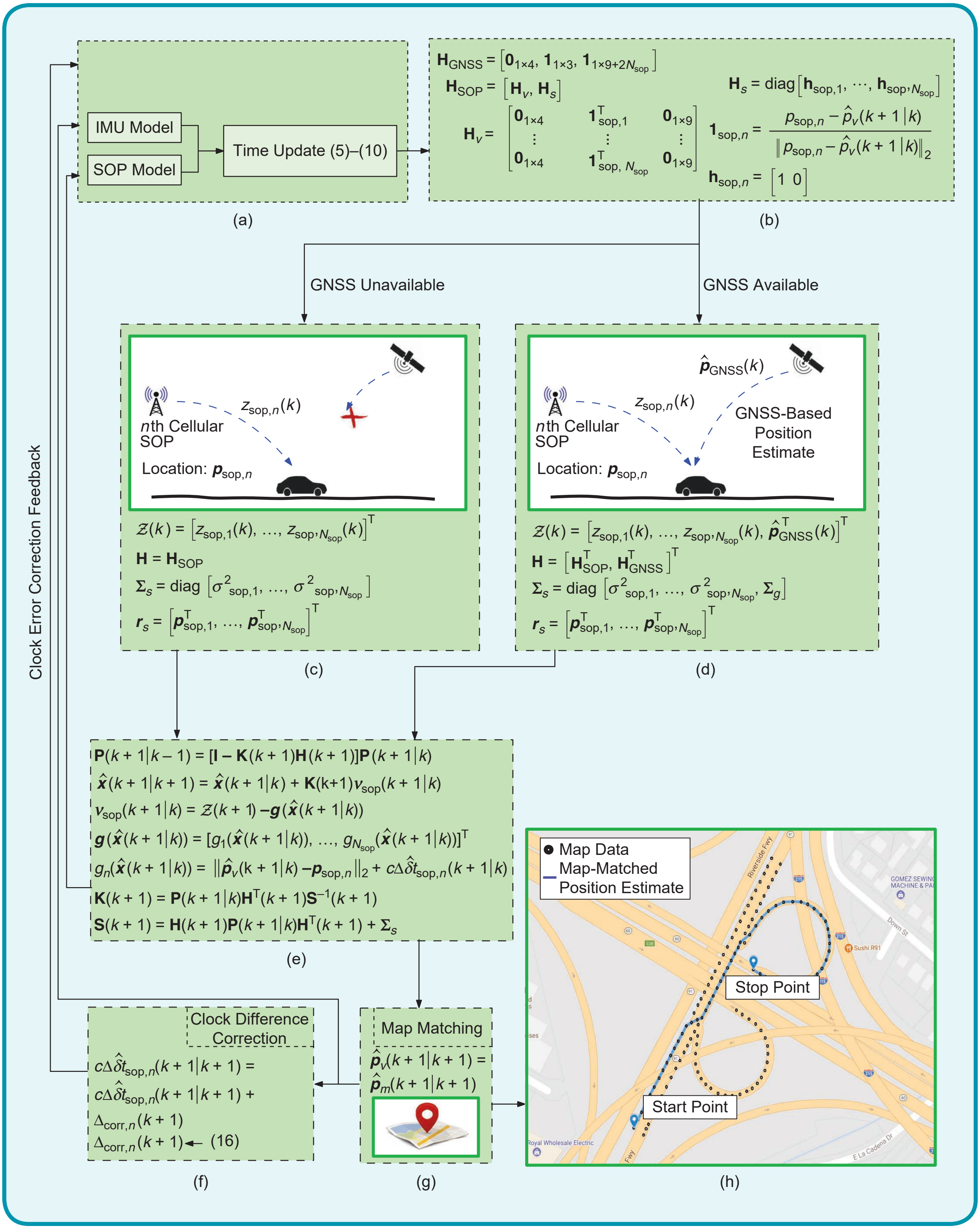

FIG 3 The architecture of the proposed EKF-based approach in situations where GNSS signals are available and unavailable. (a) The EKF time update step. (b) The EKF measurement update step. (c) The measurement update without GNSS signals. (d) The measurement update with GNSS signals. (e) The corrected state estimate and associated estimation error covariance. (f) Calculating the clock difference correction. (g) Refining the vehicle's estimated position using the map data. (h) The map-matched vehicle's position estimate.

$$\hat{\boldsymbol{p}}_m(k+1|k+1) = \min_{\boldsymbol{l}_n} \| \hat{\boldsymbol{p}}_v(k+1|k+1) - \boldsymbol{l}_n \|_{\boldsymbol{\Sigma}_m}, \tag{14}$$

where

$$\begin{aligned} &\| \hat{\boldsymbol{p}}_v(k+1|k+1) - \boldsymbol{l}_n \|_{\boldsymbol{\Sigma}_m} \\ &\quad = \sqrt{[\hat{\boldsymbol{p}}_v(k+1|k+1) - \boldsymbol{l}_n]^\mathsf{T} \boldsymbol{\Sigma}_m^{-1} [\hat{\boldsymbol{p}}_v(k+1|k+1) - \boldsymbol{l}_n]}\,. \end{aligned}$$

The estimates $\hat{\boldsymbol{p}}_v(k+1|k+1)$ and $\hat{\boldsymbol{p}}_m(k+1|k+1)$ are used to refine the clock bias state estimates according to

$$c\Delta\hat{\delta}t_{\mathrm{sop},n}(k+1|k+1) \leftarrow c\Delta\hat{\delta}t_{\mathrm{sop},n}(k+1|k+1) + \Delta_{\mathrm{corr},n}(k+1), \tag{15}$$

where

$$\begin{aligned} \Delta_{\mathrm{corr},n}(k+1) = {}& \| \hat{\boldsymbol{p}}_v(k+1|k+1) - \boldsymbol{p}_{\mathrm{sop},n} \|_2 \\ & - \| \hat{\boldsymbol{p}}_m(k+1|k+1) - \boldsymbol{p}_{\mathrm{sop},n} \|_2 . \end{aligned} \tag{16}$$

Finally, the map-matched estimate $\hat{\boldsymbol{p}}_m(k+1|k+1)$ is used to replace the estimate $\hat{\boldsymbol{p}}_v(k+1|k+1)$, i.e.,

$$\hat{\boldsymbol{p}}_v(k+1|k+1) \leftarrow \hat{\boldsymbol{p}}_m(k+1|k+1).$$

Figure 3 summarizes the architecture of the proposed navigation framework.

Experimental Results

To evaluate the performance of the proposed ground vehicle navigation framework, two experimental tests were performed in 1) an urban environment in which GNSS signals become attenuated and unreliable and 2) an area where signals from only two cellular LTE towers are used. In both experiments, a ground vehicle was equipped with the following hardware and software setup:

- two consumer-grade 800/1,900-MHz cellular omnidirectional Laird antennas [51]
- a Septentrio AsteRx-i V integrated GNSS–IMU, which is equipped with a dual-antenna multifrequency GNSS receiver and a Vectornav VN-100 microelectromechanical system IMU; the AsteRx-i V enables access to the raw measurements from this IMU, which was used for the time update of the orientation, position, and velocity, as described in the "EKF Time Update" section. The carrier phase observables recorded by the Septentrio system were fused by nearby differential GPS base stations to produce the carrier phase-based RTK solution [52]. This RTK solution was used as a ground truth during postprocessing.
- a dual-channel National Instruments (NI) universal software radio peripheral (USRP) 2954R driven by GPS-disciplined oscillator (GPSDO) [53]; this was used to simultaneously down-mix and synchronously sample cellular LTE signals at 10 megasamples/s.
- a laptop computer to store the sampled cellular signals; these samples were then processed by the Multichannel Adaptive Transceiver Information Extractor (MATRIX) software-defined radio (SDR) [12], [53], [54], which was developed by the Autonomous Systems Perception, Intelligence, and Navigation Laboratory at the University of California, Riverside.

In both experiments, the ground vehicle was assumed to have initial access to GNSS signals. This enabled estimating the initial difference between the vehicle-mounted receiver's clock bias and the clock biases of each LTE eNodeB in the environment $\{\Delta\hat{\boldsymbol{x}}_{\mathrm{clk,sop},n}(0|-1)\}_{n=1}^{N_{\mathrm{sop}}}$. Moreover, the initial estimates of the vehicle's orientation ${}^{I}_{G}\hat{\bar{\boldsymbol{q}}}_v(0|-1)$, position $\hat{\boldsymbol{p}}_v(0|-1)$, and velocity $\hat{\dot{\boldsymbol{p}}}_v(0|-1)$ were obtained from the GNSS–IMU system. The gyroscopes' and accelerometers' bias estimates, $\hat{\boldsymbol{b}}_g(0|-1)$ and $\hat{\boldsymbol{b}}_a(0|-1)$, respectively, were initialized by averaging 5 s of gravity-compensated IMU measurements at a sampling period of $T = 0.01$ s while the vehicle was stationary. It is important to note that the IMU had been running for several minutes before the samples were collected and that the temperature was near a steady-state value. The temperature was assumed to be constant during the 5-s averaging period. Any initialization error caused by this assumption is expected to be small and is captured in the initial estimation error covariance settings. The original uncertainties associated with these state estimates were set to $\mathbf{P}_{{}^{I}_{G}\bar{\boldsymbol{q}}_v}(0|-1) = (1\times10^{-3})\mathbf{I}_{3\times3}$; $\mathbf{P}_{\boldsymbol{p}_v}(0|-1) = \mathrm{blkdiag}[3\,\mathbf{I}_{2\times2},\ 0]$; $\mathbf{P}_{\dot{\boldsymbol{p}}_v}(0|-1) = \mathrm{blkdiag}[0.5\,\mathbf{I}_{2\times2},\ 0]$, $\mathbf{P}_{\boldsymbol{b}_g}(0|-1) = (3.75\times10^{-9})\mathbf{I}_{3\times3}$; $\mathbf{P}_{\boldsymbol{b}_a}(0|-1) = (9.6\times10^{-5})\mathbf{I}_{3\times3}$; and $\mathbf{P}_{\Delta\boldsymbol{x}_{\mathrm{clk,sop},n}}(0|-1) = \mathrm{diag}[3, 0.3]$, where $\mathrm{blkdiag}(\cdot)$ and $\mathrm{diag}(\cdot)$ denote a block–diagonal and a diagonal matrix, respectively. The value of $\boldsymbol{\Sigma}_g$ is set to $[5, 5, 5]\,\mathrm{m}^2$, and the SOP measurement noise variances are calculated empirically while the vehicle has access to GNSS signals according to

$$\sigma^2_{\mathrm{sop},n} \approx \frac{1}{k_{\mathrm{cutoff}}} \sum_{k=0}^{k_{\mathrm{cutoff}}-1} \hat{v}'^{\,2}_{\mathrm{sop},n}(k),$$

where k_{cutoff} is the time GNSS signals were cut off, and

$$\hat{v}'_{\mathrm{sop},n}(k) \triangleq z_{\mathrm{sop},n}(k) - \| \hat{\boldsymbol{p}}_{\mathrm{GNSS}}(k) - \boldsymbol{p}_{\mathrm{sop},n} \|_2 - c\hat{\Delta}\delta t_{\mathrm{sop},n}. \tag{17}$$

Note that (17) assumes that $\hat{v}'_{\mathrm{sop},n}$ is a stationary white sequence. However, in practice, these processes are not necessarily white, and therefore a variance inflation factor is needed to account for the colored noise. Hence, $\sigma^2_{\mathrm{sop},n} \leftarrow \alpha\sigma^2_{\mathrm{sop},n}$, where α is the inflation factor, which was chosen to be two for the experiments presented in this article. The following sections present the navigation results in each of the two environments.

Environment 1

The first experiment was conducted in an urban environment: downtown Riverside. The vehicle traversed a trajectory of 1,380 m in 190 s. The traversed trajectory within this environment is surrounded by tall trees and buildings that attenuate received cellular and GNSS signals. Due to the low elevation angles of cellular towers compared to GNSS satellites, LOS obstructions (e.g., buildings, trees, poles, other vehicles, and so on) between the tower and the vehicle-mounted receiver are prevalent. Figure 4 shows the environment and the experimental hardware setup. Through the course of the experiment, the receiver was listening to five eNodeBs corresponding to the U.S. cellular provider AT&T, with the characteristics summarized in Table 1.

It has been shown that the pseudorange measurement noise variance and multipath error are lower for signals with a higher transmission bandwidth [12]. Therefore, LTE signals with a 20-MHz bandwidth can provide more accurate pseudorange measurements compared to LTE signals with a 10-MHz bandwidth. Note that the transmission

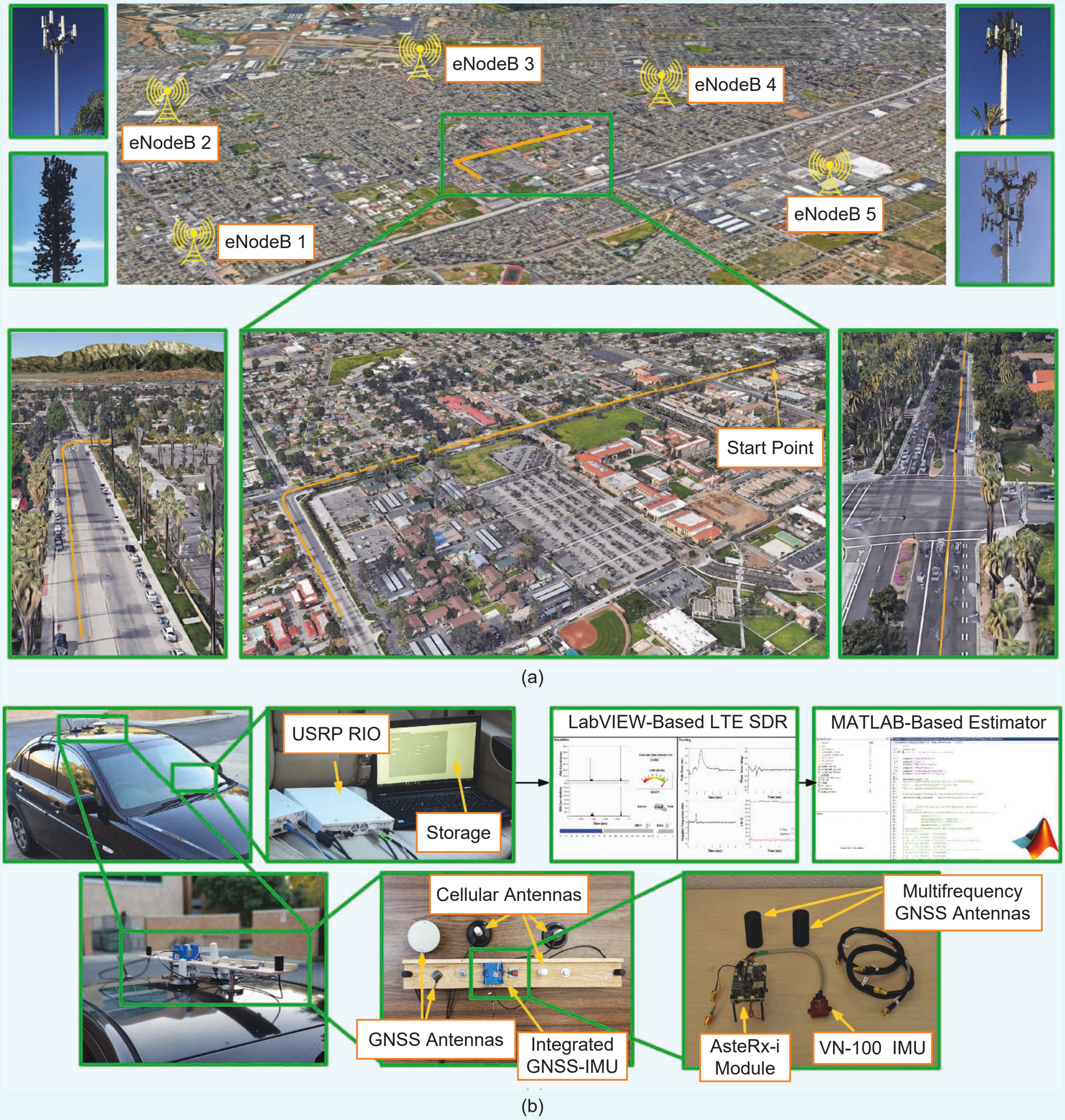

FIG 4 The experimental environment and experimental setup. (a) The environment layout, LTE SOP positions, and the true vehicle trajectory. The traversed path was surrounded by tall trees, and the received signal experienced a severe attenuation effect. (Source: Google Earth.) (b) The experimental hardware and software setup. The LTE antennas were connected to a dual-channel NI USRP-2954R driven by a GPSDO. The stored LTE signals were processed via the MATRIX SDR.

bandwidth of LTE signals is not unique and depends on the LTE network provider. Figure 5(a) shows the LTE pseudorange (solid lines) and actual range (dashed lines) variations, and Figure 5(b) provides the empirical CDF of LTE pseudoranges for eNodeB 1–5. The standard deviations of the pseudoranges for eNodeB 1–5 were calculated to be 9.19, 3.61, 4.18, 7.75, and 6.01 m, respectively. It is worth noting that one cannot fairly compare the results of these eNodeBs with each other since the received signals from these eNodeBs have experienced different carrier-to-noise ratio and multipath conditions.

The performance of the proposed navigation framework is studied in two scenarios. The first one compares the performance against three existing approaches:

- *GPS only*: This emulates a low-cost technology, which uses only GPS pseudoranges to estimate the vehicle's states.
- *GPS–IMU*: This approach fuses GPS-produced positions with an IMU, which exhibits $< 10^\circ$/h of gyroscope bias stability (such an IMU is typically considered tactical-grade) in a loosely coupled fashion to estimate the vehicle's state.
- *GPS–IMU–map matching*: This emulates an existing high-end vehicular navigation system, which map-matches the estimated vehicle's position from the GPS–IMU system produced in the second approach.

The second scenario studies the performance of the proposed framework in the absence of GNSS signals. To this end, the GPS navigation solution $\hat{\boldsymbol{p}}_{\text{GNSS}}$ was discarded in a portion of the vehicle's trajectory to emulate GNSS unavailability (see Figure 3).

Throughout the experimental test, the postprocessing software development kit was configured to produce a navigation solution at 1 Hz from GPS Level 1C/A measurements to emulate only a low-cost, low-quality GPS receiver. In contrast, the ground truth against which the proposed framework and the three previously discussed approaches were compared was produced with the expensive high-end GNSS–IMU RTK Septentrio AsteRx-i V system.

Scenario 1: Comparison Against Existing Technologies

In the first scenario, GPS signals were available along the entire trajectory. Figure 6 shows the vehicle's ground truth trajectory versus its estimated trajectory from GPS-only and GPS–IMU sources as well as the proposed framework. Table 2 compares the navigation performance of the proposed framework versus that of the three approaches: GPS only, GPS–IMU, and GPS–IMU–map. It can be seen from these results that the proposed framework outperforms all three approaches. Most notably, the proposed framework, which incorporated a standard GPS receiver whose navigation solution was loosely coupled with cellular pseudoranges and closed-loop map matching, outperforms a high-end vehicular navigation system that uses an expensive tightly coupled GPS–IMU system with map matching.

Table 1. The LTE eNodeB characteristics used in environment 1.

eNodeB	Carrier Frequency (MHz)	Cell Identification	Bandwidth (MHz)
1	1,955	216	20*
2	739	319	10
3	739	288	10
4	739	151	10
5	739	232	10

*Here, 1,024 middle subcarriers were used instead of 2,048.

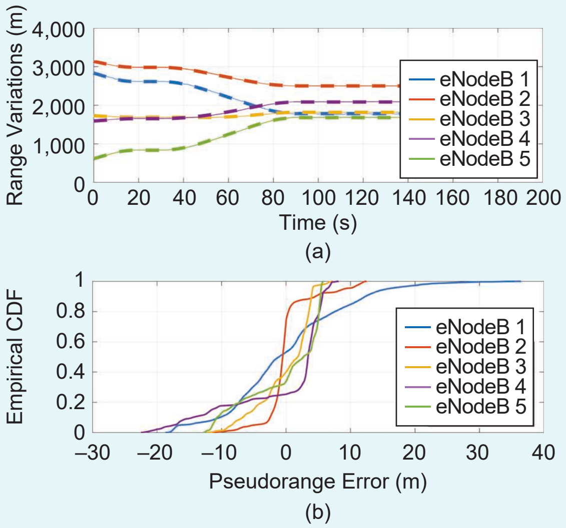

FIG 5 The (a) LTE pseudorange (solid lines) and actual range (dashed lines) variations and (b) the empirical cumulative distribution function (CDF) of the LTE pseudoranges for eNodeB 1–5.

Note the sharp change of direction in the proposed framework's trajectory (yellow curve) in Figure 6(b). This is due to a correction during the map-matching stage, which usually happens at crossroads; however, this affects only a few time steps and gets resolved after passing the crossroad.

Scenario 2: Performance When GNSS Signals Are Unavailable

In this scenario, the proposed framework's performance in the absence of GNSS signals was evaluated. To this end, the navigation solution obtained from the GPS receiver was discarded from the total trajectory for 330 m to emulate GPS unavailability. Figure 7 illustrates the portion of the vehicle's trajectory where GPS signals were unavailable. The vehicle's estimated trajectory from the proposed framework is also shown versus the vehicle's estimated trajectory from the GPS–IMU system. To differentiate the influence of the map matching from the use of LTE measurements, the GPS–IMU–LTE solution (i.e., the proposed framework without map matching) is also demonstrated in

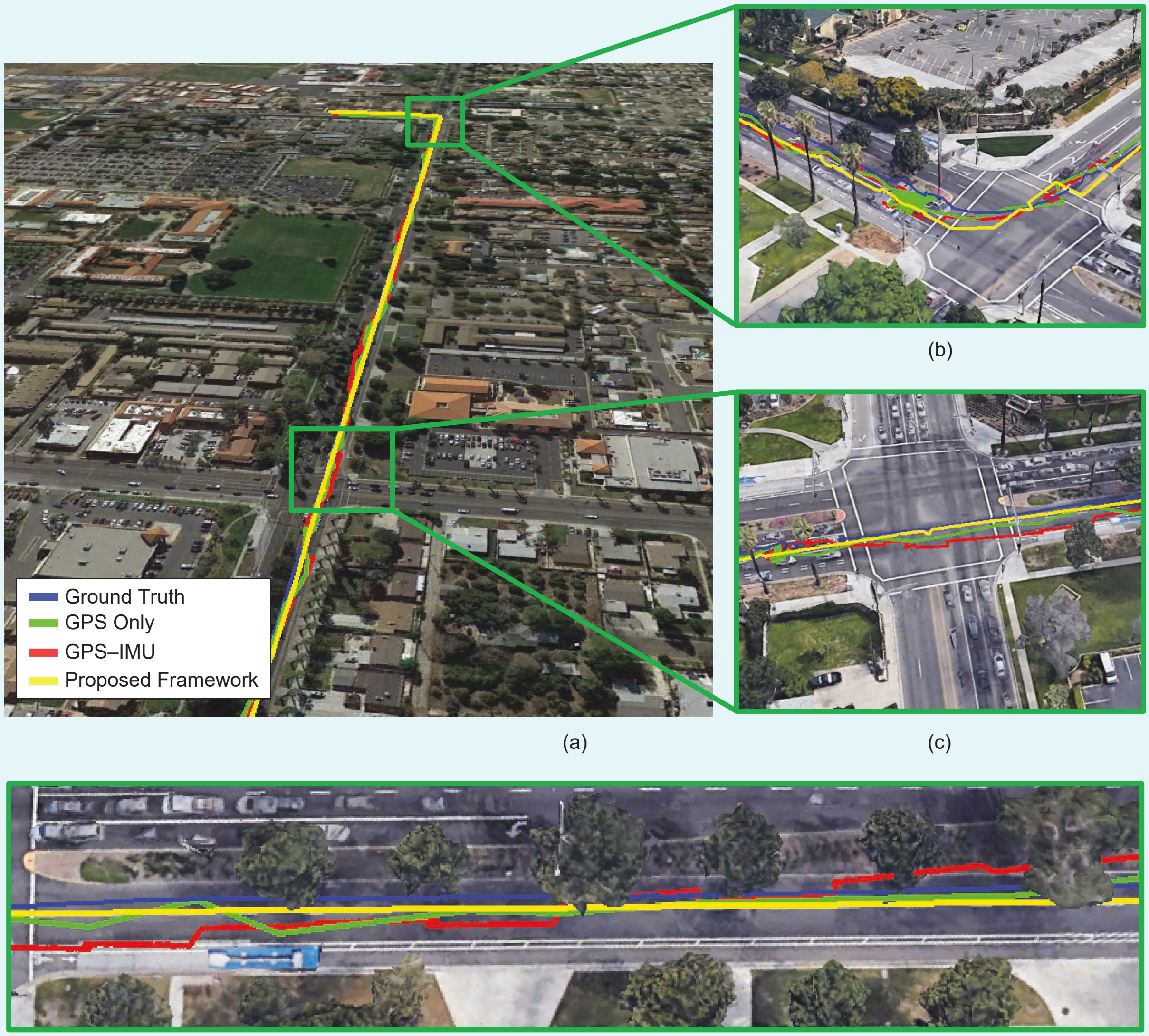

(a) (b) (c) (d)

FIG 6 (a)–(d) The experimental results in an urban environment. The vehicle's estimated trajectory with our proposed framework is compared against the estimated trajectory with GPS-only and GPS–IMU systems. The ground truth was obtained with an expensive GPS–IMU system with RTK. Experimental results indicate a 2.8-m RMSE for the proposed approach. (a) The overall trajectory. (b) A turn segment at a crossroad. (c) A straight segment at a crossroad. (d) A straight segment surrounded by tall trees. (Source: Google Earth.)

Table 2. The navigation performance comparison in an urban environment.

Navigation Solution	Position RMSE	Mean Distance Error	Maximum Distance Error
GPS only	5.61 m	6.18 m	13.3 m
GPS–IMU	4.01 m	4.53 m	10.38 m
GPS–IMU–map	3.03 m	3.54 m	8.4 m
Proposed framework	2.8 m	3.41 m	8.09 m
Improvement over GPS–IMU	30.17%	24.72%	22.06%

Figure 7. Table 3 compares the navigation performance of the proposed framework versus that of the GPS–IMU and GPS–IMU–LTE systems.

The following may be concluded from this test scenario. First, as expected, when GPS signals were unavailable, the IMU's solution drifted due to the lack of assistive corrections from GPS signals (red line in Figure 7). Note that the vehicle came to a stop at the traffic light for 9 s, during which the IMU's solution drifted forward and to the right. Subsequently, the IMU's solution continued to drift after the vehicle resumed its forward motion. This error accumulation is particularly hazardous for semi- and fully autonomous

FIG 7 The vehicle's estimated trajectory from the GPS–IMU system versus the proposed framework when GPS signals become unavailable and then available. As can be seen, the GPS–IMU solution drifts in the absence of GPS signals. In contrast, the proposed framework does not exhibit such drift, as cellular signals are used as an aiding source to the IMU. (Source: Google Earth.)

ground vehicles. In contrast, the GPS–IMU–LTE solution (green line in Figure 7) did not exhibit such drift, as cellular signals were used as an assistive source to the IMU. Second, the effect of map matching on the achieved accuracy can be investigated by comparing the GPS–IMU–LTE solution and the proposed method (yellow line in Figure 7). It is evident that the proposed framework improves the GPS–IMU–LTE solution. The estimated position RMSE using the GPS–IMU–LTE solution was found to be 4.13 m, whereas the estimated position RMSE using the proposed framework was 3.12 m.

Table 3. The navigation performance comparison without GPS signals.

Navigation Solution	Position RMSE	Mean Distance Error	Maximum Distance Error
GPS–IMU	8.37 m	14.87 m	57.12 m
GPS–IMU–LTE	4.13 m	5.66 m	12.38 m
Proposed framework	3.12 m	4.22 m	10.67 m
Improvement over GPS–IMU	62.72%	71.6%	81.32%

Table 4. The LTE eNodeB characteristics used in environment 2.

LTE SOP	Operator	Carrier Frequency (MHz)	Cell Identification	Bandwidth (MHz)
1	T-Mobile	2,145	79	20
2	AT&T	1,955	350	20

Environment 2

To assess the performance of the proposed framework in the case where a small number of cellular towers is available, the second experiment was performed in a deep urban environment in downtown Riverside, where GNSS and LTE signals experienced severe multipath and the vehicle encountered 15 s of a GNSS unavaiability condition. In this test, the vehicle traversed a 345-m trajectory while simultaneously listening to two LTE SOPs corresponding to the U.S. cellular providers T-Mobile and AT&T. Table 4 summarizes the LTE eNodeB characteristics used in experiment 2.

Figure 8 shows the experimental environment, the location of the LTE towers, and the vehicle's ground truth trajectory versus those estimated with the proposed framework and those estimated with the GPS–IMU system. To evaluate the performance of the proposed framework in the GNSS-cutoff condition, the navigation solution obtained from the GPS receiver is discarded during 40 m of the total trajectory to emulate GPS unavailability. Table 5 summarizes the navigation performance in this environment. It can be seen that the proposed approach yielded a 32% reduction in the position RMSE and a 43% decrease in the maximum distance error despite using a very limited number of cellular SOPs. For a comparative analysis, the results achieved by the proposed framework were compared with those produced by the particle-filter-based framework without using an IMU, presented in [19]. The method presented in [19] achieved a maximum error of 11.7 m across a trajectory of 345 m, while the maximum error obtained by the proposed

FIG 8 (a)–(c) The second experimental environment layout, including LTE SOP tower locations, the true vehicle trajectory, and the different navigation solutions, where the estimated vehicle position obtained from the GPS–IMU method and the proposed framework are shown using yellow and red lines, respectively. In this experiment, the vehicle-mounted receiver traversed 345 m across urban streets while simultaneously listening to only two LTE SOPs. It is worth mentioning that in the experiment area, the LTE towers were obstructed by buildings. The first LTE tower was far from the vehicle, and a large portion of the car's trajectory had no clear LOS to it. As can be seen, the estimated position using the proposed framework closely follows the ground truth trajectory during the drive. Experimental results indicate a 3.43-m RMSE for the proposed approach. (a) The environment layout showing the vehicle's trajectory and eNodeB locations. (b) A top view of the vehicle trajectory. (c) A camera angle showing the GPS-IMU solution drifting in the absence of GPS signals. Even after GPS returns, the GPS-IMU system performs poorly after the turn due to multipath. (Source: Google Earth.)

Table 5. The navigation performance comparison without GPS signals.

Navigation Solution	Position RMSE	Mean Distance Error	Maximum Distance Error
GPS–IMU	5.1 m	4.75 m	8.96 m
Proposed framework	3.43 m	4.18 m	5.03 m
Improvement over GPS–IMU	32%	18%	43%

framework was 5.03 m for the same trajectory. Hence, as expected, incorporating an IMU in the EKF-based framework significantly reduced the maximum error.

Conclusions and Future Work

This article presented a novel framework for vehicular navigation in urban environments. The framework uses an IMU, cellular signals, and GNSS signals (when available) along with closed-loop map matching. On the one hand, when GNSS signals are unavailable, the proposed framework uses cellular signals and map data as assistive sources to the IMU, bounding the IMU drift and producing an accurate estimate of the vehicle's state. On the other hand, when GNSS signals are available, the proposed framework fuses estimates from the GNSS receiver with cellular measurements to produce an estimate that is within a few meters of the solution produced by a very expensive high-end GNSS–IMU system with RTK and map matching.

Experimental results in two urban environments are presented, demonstrating the accuracy of the proposed framework versus existing technologies. It was shown that the proposed framework achieved a position RMSE of 2.8 m across a trajectory of 1,380 m while GNSS signals were available and a position RMSE of 3.12 across the same trajectory while GNSS signals were not available for 330 m. In addition, the robustness of the proposed framework against a limited number of cellular towers (only two) was demonstrated, showing a position RMSE of 3.43 m across a trajectory of 345 m where GNSS signals were unavailable for 40 m. While this article considered a map displacement error with a zero-mean random vector, more sophisticated map models could be investigated in future work in an attempt to improve the robustness of the framework against unmodeled map errors.

Acknowledgments

This work was supported in part by the Office of Naval Research, under grants N00014-16-1-2305 and N00014-16-1-2809, and the National Science Foundation, under grants 1929571 and 1929965.

About the Authors

Zaher (Zak) M. Kassas earned his B.E. degree in electrical engineering from the Lebanese American University, Beirut, Lebanon; his M.S. degree in electrical and computer engineering from The Ohio State University, Columbus; his M.S.E. degree in aerospace engineering; and his Ph.D. degree in electrical and computer engineering from the University of Texas at Austin. He is an assistant professor at the University of California, Irvine and the director of the Autonomous Systems Perception, Intelligence, and Navigation Laboratory, University of California, Irvine. In 2018, he received the National Science Foundation (NSF) Faculty Early Career Development Program (CAREER) award, and in 2019, he received the Office of Naval Research (ONR) Young Investigator Program (YIP) award. He is a recipient of 2018 IEEE Walter Fried Award, 2018 Institute of Navigation (ION) Samuel Burka Award, and 2019 ION Col. Thomas Thurlow Award. He is an associate editor for *IEEE Transactions on Aerospace and Electronic Systems* and *IEEE Transactions on Intelligent Transportation Systems*. His research interests include cyber-physical systems, estimation theory, navigation systems, autonomous vehicles, and intelligent transportation systems.

Mahdi Maaref earned his B.E degree in electrical engineering and his M.Sc. degree in electrical engineering-power systems from the University of Tehran, Iran, in 2008 and 2011, respectively, and his Ph.D. degree in electrical engineering at Shahid Beheshti University, Tehran, in 2016. He is a postdoctoral research fellow at the University of California, Irvine and a member of the Autonomous Systems Perception, Intelligence, and Navigation Laboratory, University of California, Irvine. Previously, he was a visiting research collaborator at the University of Alberta, Edmonton, Canada, in 2016. His research interests include autonomous ground vehicles, opportunistic perception, and autonomous integrity monitoring.

Joshua J. Morales earned his B.S. degree in electrical and computer engineering with high honors from the University of California, Riverside. He is a Ph.D. degree candidate at the University of California, Irvine and a member of the Autonomous Systems Perception, Intelligence, and Navigation Laboratory, University of California, Irvine. His research interests include estimation, navigation, autonomous vehicles, and intelligent transportation systems. He is a Student Member of the IEEE.

Joe J. Khalife earned his B.E. degree in electrical engineering and his M.S. degree in computer engineering from the Lebanese American University, Beirut, Lebanon. He is a Ph.D. degree candidate at the University of California, Irvine and a member of the Autonomous Systems Perception, Intelligence, and Navigation Laboratory, University of California, Irvine. His research interests include opportunistic navigation, autonomous vehicles, and software-defined radio. He is a Student Member of the IEEE.

Kimia Shamaei earned her B.S. and M.S. degrees in electrical engineering from the University of Tehran, Iran. She is a Ph.D. degree candidate at the University of California, Irvine and a member of the Autonomous Systems Perception, Intelligence, and Navigation Laboratory, University of California, Irvine. Her research interests include the analysis and modeling of signals of opportunity and software-defined radio. She is a Student Member of the IEEE.

References

[1] N. Zhu, J. Marais, D. Betaille, and M. Berbineau, "GNSS position integrity in urban environments: A review of literature," *IEEE Trans. Intell. Transp. Syst.*, vol. 19, no. 9, pp. 2762–2778, Jan. 2018. doi: 10.1109/TITS.2017.2766768.

[2] Q. Sun and J. Zhang, “RAIM method for improvement on GNSS reliability and integrity,” in *Proc. IEEE/AIAA 28th Digital Avionics Systems*, Oct. 2009, pp. 3–11. doi: 10.1109/DASC.2009.5347420.

[3] R. Toledo-Moreo, D. Betaille, and F. Peyret, “Lane-level integrity provision for navigation and map matching with GNSS, dead reckoning, and enhanced maps,” *IEEE Trans. Intell. Transp. Syst.*, vol. 11, no. 1, pp. 100–112, Mar. 2010. doi: 10.1109/TITS.2009.2031625.

[4] M. Maaref, J. Khalife, and Z. Kassas, “Integrity monitoring of LTE signal of opportunity-based navigation for autonomous ground vehicles,” in *Proc. ION GNSS+ Conf.*, Sept. 2018, pp. 2456–2466.

[5] M. Rohani, D. Gingras, and D. Gruyer, “A novel approach for improved vehicular positioning using cooperative map matching and dynamic base station DGPS concept,” *IEEE Trans. Intell. Transp. Syst.*, vol. 17, no. 1, pp. 230–239, Jan. 2016. doi: 10.1109/TITS.2015.2465141.

[6] M. Hashemi, “Reusability of the output of map-matching algorithms across space and time through machine learning,” *IEEE Trans. Intell. Transp. Syst.*, vol. 18, no. 11, pp. 3017–3026, Nov. 2017. doi: 10.1109/TITS.2017.2669085.

[7] J. Morales, J. Khalife, and Z. Kassas, “Opportunity for accuracy,” *GPS World Mag.*, vol. 27, no. 3, pp. 22–29, Mar. 2016.

[8] Z. Kassas, J. Morales, K. Shamaei, and J. Khalife, “LTE steers UAV,” *GPS World Mag.*, vol. 28, no. 4, pp. 18–25, Apr. 2017.

[9] A. Ramanandan, A. Chen, and J. Farrell, “Inertial navigation aiding by stationary updates,” *IEEE Trans. Intell. Transp. Syst.*, vol. 13, no. 1, pp. 235–248, Mar. 2012. doi: 10.1109/TITS.2011.2168818.

[10] A. Vu, A. Ramanandan, A. Chen, J. Farrell, and M. Barth, “Real-time computer vision/DGPS-aided inertial navigation system for lane-level vehicle navigation,” *IEEE Trans. Intell. Transp. Syst.*, vol. 13, no. 2, pp. 899–913, June 2012. doi: 10.1109/TITS.2012.2187641.

[11] Z. He, S. Xi-wei, L. Zhuang, and P. Nie, “Online map-matching framework for floating car data with low sampling rate in urban road networks,” *IET Intell. Transp. Syst.*, vol. 7, no. 4, pp. 404–414, Dec. 2013. doi: 10.1049/iet-its.2011.0226.

[12] K. Shamaei and Z. Kassas, “LTE receiver design and multipath analysis for navigation in urban environments,” *Navigation*, vol. 65, no. 4, pp. 655–675, Dec. 2018. doi: 10.1002/navi.272.

[13] R. Mohamed, H. Aly, and M. Youssef, “Accurate real-time map matching for challenging environments,” *IEEE Trans. Intell. Transp. Syst.*, vol. 18, no. 4, pp. 847–857, Apr. 2017. doi: 10.1109/TITS.2016.2591958.

[14] G. Jagadeesh and T. Srikanthan, “Online map-matching of noisy and sparse location data with hidden Markov and route choice models,” *IEEE Trans. Intell. Transp. Syst.*, vol. 18, no. 9, pp. 2423–2434, Sept. 2017. doi: 10.1109/TITS.2017.2647967.

[15] M. Najjar and P. Bonnifait, “A road-matching method for precise vehicle localization using belief theory and Kalman filtering,” *Autonom. Robots*, vol. 19, no. 2, pp. 173–191, Sept. 2005. doi: 10.1007/s10514-005-0609-1.

[16] M. Yu, Z. Li, Y. Chen, and W. Chen, “Improving integrity and reliability of map matching techniques,” *J. Global Position. Syst.*, vol. 5, no. 10, pp. 40–46, Dec. 2006. doi: 10.5081/jgps.5.1.40.

[17] M. Quddus, W. Ochieng, and R. Noland, “Current map-matching algorithms for transport applications: State-of-the art and future research directions,” *Transp. Res. C, Emerg. Technol.*, vol. 15, no. 5, pp. 312–328, May 2007. doi: 10.1016/j.trc.2007.05.002.

[18] K. Zhang, S. Liu, Y. Dong, D. Wang, Y. Zhang, and L. Miao, “Vehicle positioning system with multi-hypothesis map matching and robust feedback,” *IET Intell. Transp. Syst.*, vol. 11, no. 10, pp. 649–658, Nov. 2017. doi: 10.1049/iet-its.2017.0072.

[19] M. Maaref and Z. Kassas, “Ground vehicle navigation in GNSS-challenged environments using signals of opportunity and a closed-loop map-matching approach,” *IEEE Trans. Intell. Transp. Syst.*, to be published. doi: 10.1109/TITS.2019.2907851.

[20] T. Braunl, “Localization and navigation,” in *Embedded Robotics*. Berlin: Springer-Verlag, 2008, pp. 241–269.

[21] T. Walter, P. Enge, J. Blanch, and B. Pervan, “Worldwide vertical guidance of aircraft based on modernized GPS and new integrity augmentations,” *Proc. IEEE*, vol. 96, no. 12, pp. 1918–1935, Dec. 2008. doi: 10.1109/JPROC.2008.2006099.

[22] M. Joerger, L. Gratton, B. Pervan, and C. Cohen, “Analysis of Iridium-augmented GPS for floating carrier phase positioning,” *Navigation*, vol. 57, no. 2, pp. 137–160, 2010. doi: 10.1002/j.2161-4296.2010.tb01773.x.

[23] S. Peyraud et al., “About non-line-of-sight satellite detection and exclusion in a 3-D map-aided localization algorithm,” *Sensors*, vol. 13, no. 1, pp. 829–847, Jan. 2013. doi: 10.3390/s130100829.

[24] X. Chen, F. Dovis, S. Peng, and Y. Morton, “Comparative studies of GPS multipath mitigation methods performance,” *IEEE Trans. Aerosp. Electron. Syst.*, vol. 49, no. 3, pp. 1555–1568, July 2013. doi: 10.1109/TAES.2013.6558004.

[25] P. Strode and P. Groves, “GNSS multipath detection using three-frequency signal-to-noise measurements,” *GPS Sol.*, vol. 20, no. 3, pp. 399–412, July 2016. doi: 10.1007/s10291-015-0449-1.

[26] “Physical layer standard for cdma2000 spread spectrum systems (C.S0002-E),” 3rd Generation Partnership Project 2 (3GPP2), Arlington, VA, TS C.S0002-E, June 2011.

[27] J. Khalife, K. Shamaei, and Z. Kassas, “A software-defined receiver architecture for cellular CDMA-based navigation,” in *Proc. IEEE/ION Position, Location, and Navigation Symp.*, Apr. 2016, pp. 816–826.

[28] J. Khalife, K. Shamaei, and Z. Kassas, “Navigation with cellular CDMA signals—Part I: Signal modeling and software-defined receiver design,” *IEEE Trans. Signal Process.*, vol. 66, no. 8, pp. 2191–2203, Apr. 2018. doi: 10.1109/TSP.2018.2799167.

[29] “Evolved universal terrestrial radio access (E-UTRA); physical channels and modulation,” 3rd Generation Partnership Project (3GPP), Sophia Antipolis, France, TS 36.211, Jan. 2011. [Online]. Available: http://www.3gpp.org/ftp/Specs/html-info/36211.htm

[30] K. Shamaei, J. Khalife, and Z. Kassas, “Performance characterization of positioning in LTE systems,” in *Proc. 29th Int. Tech. Meeting .Satellite Division Institute Navigation (ION GNSS+2016)*, Sept. 2016, pp. 2262–2270.

[31] K. Shamaei, J. Khalife, and Z. Kassas, “Comparative results for positioning with secondary synchronization signal versus cell specific reference signal in LTE systems,” in *Proc. ION Int. Tech. Meeting Conf.*, Jan. 2017, pp. 1256–1268.

[32] F. Knutti, M. Sabathy, M. Driusso, H. Mathis, and C. Marshall, “Positioning using LTE signals,” in *Proc. Navigation Conf. Europe*, Apr. 2015, pp. 1–8.

[33] K. Shamaei, J. Khalife, and Z. Kassas, “Exploiting LTE signals for navigation: Theory to implementation,” *IEEE Trans. Wireless Commun.*, vol. 17, no. 4, pp. 2173–2189, Apr. 2018. doi: 10.1109/TWC.2018.2789882.

[34] M. Driusso, C. Marshall, M. Sabathy, F. Knutti, H. Mathis, and F. Babich, “Vehicular position tracking using LTE signals,” *IEEE Trans. Veh. Technol.*, vol. 66, no. 4, pp. 3376–3391, Apr. 2017. doi: 10.1109/TVT.2016.2589463.

[35] J. del Peral-Rosado et al., “Software-defined radio LTE positioning receiver towards future hybrid localization systems,” in *Proc. Int. Communication Satellite Systems Conf.*, Oct. 2013, pp. 14–17. doi: 10.2514/6.2013-5610.

[36] K. Shamaei, J. Khalife, S. Bhattacharya, and Z. Kassas, “Computationally efficient receiver design for mitigating multipath for positioning with LTE signals,” in *Proc. 30th Int. Tech. Meeting Satellite Division Institute Navigation (ION GNSS+ 2017)*, Sept. 2017, pp. 3751–3760.

[37] R. Zekavat and R. Buehrer, *Handbook of Position Location: Theory, Practice and Advances*, 1st ed. Hoboken, NJ: Wiley-IEEE Press, 2011.

[38] Z. Kassas, “Analysis and synthesis of collaborative opportunistic navigation systems,” Ph.D. dissertation, The University of Texas at Austin, 2014.

[39] Z. Kassas, V. Ghadiok, and T. Humphreys, “Adaptive estimation of signals of opportunity,” in *Proc. 27th Int. Tech. Meeting Satellite Division Institute Navigation (ION GNSS+ 2014)*, Sept. 2014, pp. 1679–1689.

[40] J. Morales and Z. Kassas, “Optimal collaborative mapping of terrestrial transmitters: receiver placement and performance characterization,” *IEEE Trans. Aerosp. Electron. Syst.*, vol. 54, no. 2, pp. 992–1007, Apr. 2018. doi: 10.1109/TAES.2017.2773238.

[41] J. Khalife and Z. Kassas, “Navigation with cellular CDMA signals—Part II: Performance analysis and experimental results,” *IEEE Trans. Signal Process.*, vol. 66, no. 8, pp. 2204–2218, Apr. 2018. doi: 10.1109/TSP.2018.2799166.

[42] “Recommended minimum performance standards for cdma2000 spread spectrum base stations,” 3GPP2, Arlington, VA, Rep. no.: C.S0010-B, Rep. no.: C.S0010-B, Dec. 1999. [Online]. Available: https://www.3gpp2.org/Public_html/Specs/C.S0010-B_v2.0_021704.pdf

[43] Z. Kassas and T. Humphreys, “Observability analysis of collaborative opportunistic navigation with pseudorange measurements,” *IEEE Trans. Intell. Transp. Syst.*, vol. 15, no. 1, pp. 260–273, Feb. 2014. doi: 10.1109/TITS.2013.2278293.

[44] R. Brown and P. Hwang, *Introduction to Random Signals and Applied Kalman Filtering*, 3rd ed. New York: Wiley, 2002.

[45] Y. Bar-Shalom, X. Li, and T. Kirubarajan, *Estimation with Applications to Tracking and Navigation*. New York: Wiley, 2002.

[46] A. Thompson, J. Moran, and G. Swenson, *Interferometry and Synthesis in Radio Astronomy*, 2nd ed. New York: Wiley, 2001.

[47] M. Atia et al., “A low-cost lane-determination system using GNSS/IMU fusion and HMM-based multistage map matching,” *IEEE Trans. Intell. Transp. Syst.*, vol. 18, no. 11, pp. 3027–3037, Nov. 2017. doi: 10.1109/TITS.2017.2672541.

[48] Open Street Map foundation (OSMF). Accessed on: Apr. 10, 2018. [Online]. Available: https://www.openstreetmap.org

[49] J. Farrell and M. Barth, *The Global Positioning System and Inertial Navigation*. New York: McGraw-Hill, 1998.

[50] P. Groves, *Principles of GNSS, Inertial, and Multisensor Integrated Navigation Systems*, 2nd ed. Norwood, MA: Artech House, 2013.

[51] “Laird phantom 3G/4G multiband antenna NMO mount white TRA6927M-3NB,” Laird Connectivity, Akron, OH. [Online]. Available: https://www.lairdtech.com/products/phantom-series-antennas

[52] “AsteRx-i V,” Septentrio, Leuven, Belgium, 2018. [Online]. Available: https://www.septentrio.com/products

[53] “Universal software radio peripheral-2954r,” National Instruments, Austin, TX. [Online]. Available: http://www.ni.com/en-us/support/model.usrp-2954.html

[54] Z. Kassas, J. Khalife, K. Shamaei, and J. Morales, “I hear, therefore I know where I am: Compensating for GNSS limitations with cellular signals,” *IEEE Signal Process. Mag.*, vol. 34, no. 5, pp. 111–124, Sept. 2017. doi: 10.1109/MSP.2017.2715363.